RESEARCH PAPER

# Experimental and Numerical Investigations of the Effect of Curing Conditions on the Temperature Rise of Concrete

Aleksandra Kuryłowicz-Cudowskaa[1]

## Abstract

This paper presents experimental and numerical studies investigating the impact of three curing conditions on temperature evolution in concrete cubes. The tests were performed on samples of the same volume (3.375 dm$^3$) under different curing conditions: room temperature, insulation boxes, and adiabatic calorimeter. Various cements (Portland cement, Portland composite cement, and blast furnace slag cement) and aggregates (gravel and basalt) were examined. The temperature evolution for all mixtures was analyzed, revealing a correlation between temperature increase and concrete type. Under insulation and adiabatic curing, Portland cement with gravel aggregate exhibited the highest temperature rise, while blast furnace slag cement with basalt aggregate showed the lowest increase. The incorporation of slag, ash, or other mineral additives reduced temperature rise. Additionally, basalt aggregate's higher heat capacity and thermal energy accumulation led to a decreased temperature increase compared to gravel. Using recorded thermal data, a numerical procedure predicting temperature development in nonadiabatic conditions through direct adiabatic tests is proposed. Comparisons between experimental and numerical temperature evolutions confirmed the model's accuracy.

**Keywords** Concrete temperature · Curing conditions · Hydration heat · Adiabatic calorimetry · Thermo-chemical model · Digital 1-wire sensor

## 1 Introduction

The hydration of cement is a highly exothermic reaction, necessitating the prediction and continuous on-site monitoring of the temperature rise in early-age concrete projects. It is crucial to ensure that the maximum concrete temperature, as indicated by [1], does not exceed 70 °C. The temperature differential between the interior and exterior of a concrete element significantly influences mechanical properties, including compressive strength, and can induce thermal stress-related damage [2–5]. The maximum temperature increase of in-place concrete is contingent on factors such as structure type (mass concrete, medium-massive element, thin-walled structure), environmental conditions, concrete mixture type, and curing method. Various methods, including the use of fiber-optic temperature sensors [6], have been employed by researchers to monitor the hydration process. Peak temperatures of concrete specimens with different w/c ratios were measured during these experiments, highlighting the suitability of fiber-optic temperature sensors for engineering applications [6]. Notably, Liang et al. [7] proposed a bifilar optical fiber embedding technique for internally monitoring the temperature of concrete dam structures, while [8] introduced an intelligent system for monitoring concrete pavement slabs exposed to external temperature fluctuations. The installation of fiber-optic temperature and strain sensors, along with an innovative Fabry–Perot interferometer-based optical fiber inclinometer, facilitated the monitoring and evaluation of the thermal curling process in a concrete pavement slab.

Considering curing conditions, three effective methods for determining the heat of hydration are isothermal, semi-adiabatic, and adiabatic. Isothermal and semi-adiabatic calorimetry are commonly applied to measure the heat of

✉ Aleksandra Kuryłowicz-Cudowska
  aleksandra.kurylowicz-cudowska@pg.edu.pl

1  Department of Mechanics of Materials and Structures, Faculty of Civil and Environmental Engineering, Gdańsk University of Technology, Narutowicza 11/12, 80-233 Gdańsk, Poland

🖋 Springer

hydration in paste or mortar samples, with small-volume samples tested to classify the cement nature and determine its mineralogical composition. Recent research, such as that by Frølich et al. [9] and [10], has investigated the accuracy of isothermal calorimetry measurements in predicting mortar strength and studying the long-term hydration of cement paste with fly ash-blended Portland cement, respectively. MacLeod et al. [11] explored the effects of adding carbon nanotubes to cementitious nanocomposites on early age hydration kinetics using isothermal calorimetry. In a numerical simulation by [12], the heat and mass transport during the hydration of Portland cement mortar were studied using isothermal calorimetry and semi-adiabatic experiments. However, it is important to note that predicting concrete temperature increase solely from isothermal studies does not account for changes in cement reactivity with temperature variations. This limitation makes isothermal calorimetry less representative of real concrete structure conditions, where temperatures change continuously [13]. An alternative approach involves the use of semi-adiabatic calorimeters, where heat exchange with the exterior occurs, and total heat loss should not exceed 100 J/h/K [13]. While less accurate than adiabatic tests, semi-adiabatic tests offer cost-effective alternatives widely adopted in various institutions [2, 14, 15]. According to [3], the cost of an adiabatic temperature rise test is around 1000 USD (2000 USD in certified institutions in Korea), while a semi-adiabatic test costs 660 USD (including expanded reusable polystyrene and a temperature sensor). This cost efficiency has contributed to the widespread use of semi-adiabatic tests as substitutes for adiabatic tests.

Considering reliability and accuracy, it can be asserted that adiabatic curing conditions stand out as the optimal method for predicting temperature increases, a critical aspect in concrete characterization. In adiabatic equipment, the temperature loss of the sample is minimal, not exceeding 0.02 K/h [13]. Adiabatic tests are particularly suitable for massive structures, where the limited heat loss of concrete is crucial due to low thermal conductivity, and excessive temperature rise may lead to cracks [16]. Under adiabatic conditions, the temperature evolution is influenced by the cement content, w/c ratio, and types of aggregates rather than the equipment itself [16]. Measurements of temperature increase in concrete under almost adiabatic conditions provide high accuracy, enabling adjustments to the concrete composition to preserve mechanical and physical properties in massive structures. Due to the adverse effects of thermal stresses in young concrete, there is a practical demand for engineers to assess adiabatic temperature increases across various concrete mixtures. Numerous studies have attempted to predict adiabatic temperature evolution using isothermal, semi-adiabatic, and numerical tests [2, 3, 17–19]. In turn, calorimetric tests on concrete cured under adiabatic conditions has been limited to prototypes designed in research centers [20, 21]. In a paper by [21], the own concrete adiabatic calorimeter was developed. The measured adiabatic temperature rise curve ultimately served as the basis for thermal load function in thermal analysis of two 1.2-m plain concrete cubes. The novelty of this study lies in directly employing an industrial adiabatic concrete calorimeter compliant with the EN 12390-15 [22] standard for investigation.

It is noteworthy that measurements of heat release under adiabatic conditions serve as fundamental data for estimating the temperature and strength development of young concrete [23]. The accuracy of numerical predictions for thermal evolution in hardened concrete hinges on precise input values for thermal properties, such as adiabatic temperature rise characteristics, identification of appropriate boundary conditions, and the selection of a mathematical model consistent with measurement capabilities [24, 25]. The temperature and heat measurements during concrete hardening are pivotal parameters around which hypotheses, mathematical theories, and simulation models are constructed. To explore the influence of boundary conditions on concrete temperature development, a research program was proposed, encompassing laboratory tests on concrete samples cured at room temperature in insulation boxes and an adiabatic calorimeter. This study reports on the combined effects of binder types (Portland cement, Portland composite cement with silica fly ash, granulated blast furnace slag, and blast furnace slag cement) and aggregates (gravel and basalt) on the temperature evolution of concrete under three conditions. The primary objective was to investigate identical volumes ($3.375 \text{ dm}^3$) of tested samples under all curing conditions, with the adiabatic calorimeter dedicated to 150 mm cubic concrete samples. The dimensions of specimens in insulated boxes and at room temperature were consistent (150 mm × 150 mm × 150 mm), with the volume of concrete deliberately chosen as a non-factor impacting temperature development. This non-standardized approach reflects the author's originality. Temperature measurements for cubes cured at room temperature and in insulation boxes utilized an original system with 1-wire digital sensors, while the adiabatic temperature increase was directly measured using a highly accurate adiabatic calorimeter. Finally, model parameters were identified using the results of direct adiabatic measurements to predict temperature evolution under non-adiabatic conditions.

## 2 Theoretical Formulation of the Thermal Model

The formulation of the thermal model for concrete hardening involves the relationship between heat production and cement hydration, leading to the generation of a heterogeneous temperature field through heat exchange between the interior and the environment [26, 27]. To numerically represent the concrete temperature distribution, the thermochemical model from [28] is implemented. This model, consistent with several authors [29, 30], considers heat transport solely through conduction, omitting the movement of moisture, providing a practical approach for solving engineering problems. The model includes two key formulations: the heat conduction equation expressed by Fourier's law (1) and the chemical kinetics equation as a function of the hydration degree development (2):

$$\nabla \cdot \lambda \nabla T + Q_\xi \dot{\xi} = \rho c \dot{T}, \tag{1}$$

$$\dot{\xi} = \tilde{A}(\xi) \exp\left(-\frac{E_a}{R\,T}\right)$$
$$= \underbrace{\frac{\kappa}{n_0}\left(\frac{A_0}{\kappa}\frac{1}{\xi_{\max}} + \xi\right)(\xi_{\max} - \xi)\exp\left(-\overline{n}\frac{\xi}{\xi_{\max}}\right)}_{\tilde{A}(\xi) = \overline{A}\,\eta\ \text{(normalisedchemicalaffinity)}} \underbrace{\exp\left(-\frac{E_a}{R\,T}\right)}_{\text{(Arrheniustyplaw)}}. \tag{2}$$

The phenomenon of heat transfer is controlled by the following parameters: thermal conductivity $\lambda$ (W/(m K)), internal heat source $Q_\xi$ (J/m$^3$), density $\rho$ (kg/m$^3$), specific heat $c$ (kJ/(kg K)), gas constant $R$ (J/(mol K)), and activation energy $E_a$ (J/mol). The rate of heat of hydration varies throughout the concrete hardening process. Formation of new hydrates affects the mechanical properties of concrete. Thus, a normalised internal variable, that is, the hydration degree $\xi$ (−), was introduced for predicting the advancement of the hardening process. The final hydration degree is given by [31]:

$$\xi_{\max} = 1.031\,(w/c)/(0.194 + w/c). \tag{3}$$

The initial condition can be noted by the initial temperature of the concrete mix, that is, $T_0$ (°C). Because the conductivity of concrete is relatively low, the temperature of the concrete interior increases significantly compared with that of the concrete surface. Heat is transferred between the environment and concrete through convection (Newton's condition) and radiation (Stefan–Boltzmann's condition). For simplicity, radiation is often considered in association with convection, and the heat flow from the element surface can be expressed as:

$$q_0 = \alpha_s\,(T_{\text{surf}} - T_{\text{env}}), \tag{4}$$

where $\alpha_s$ (W/(m$^2$ K)) is the heat transfer coefficient, and $T_{\text{env}}$ (°C) and $T_{\text{surf}}$ (°C) represent the ambient and surface temperature, respectively.

Under adiabatic conditions, Eq. (1) becomes $\rho c \dot{T} = Q_\xi \dot{\xi}$, and the temperature can be described by $T = T_0 + Q_\xi \xi/(\rho c)$. At the end of the adiabatic test, $T = T_{\max}$, $\xi = \xi_{\max}$, and finally, the constant $Q_\xi = \rho c\,(T_{\max} - T_0)/\xi_{\max}$. The adiabatic calorimetric test of concrete cubes allows the measurement of the normalised chemical affinity $\tilde{A}(\xi)$. The following parameters: $\kappa/n_0$ (1/h), $A_0/\kappa$ (−), and $\overline{n}$ (−) are adjusted using regression analysis by fitting the model affinity $\tilde{A}(\xi)$ to the experimental one [28]:

$$\tilde{A}_{\text{test}} = \frac{\xi_{\max}\dot{T}}{T_{\max} - T_0}\exp\left(\frac{E_a}{RT}\right). \tag{5}$$

The differential equations of heat transport ((1) and (2)) were solved using their own code and the finite difference method. In the classical approach to differential equations, the derivatives of functions are replaced with finite differences in a discretised space. The temperature field $T(x,t)$ was defined in space ($m_s$) and time domain ($n_s$), where the distance between nodes $\Delta x = L/(m_s - 1)$ depends on considered length $L$. A stable solution for explicit discretization satisfies the criterion: $\Delta t \leq \frac{\rho c}{2\lambda}(\Delta x^2)$. The starting value for the prediction can be described by:

$$T_{n,m} = T_0,\ \xi_{n,m} = 0; \tag{6}$$

hence, the rate of hydration degree is formulated by:

$$\dot{\xi}_{n,m} = \frac{\kappa}{n_0}\left(\frac{A_0}{\kappa}\frac{1}{\xi_{\max}} + \xi_{n,m}\right)(\xi_{\max} - \xi_{n,m})$$
$$\exp\left(-\overline{n}\frac{\xi_{n,m}}{\xi_{\max}}\right)\exp\left(-\frac{E_a}{RT_{n,m}}\right). \tag{7}$$

Based on the above data, the starting values for the iteration process were obtained as follows:

$$\xi_{n+1,m} = \xi_{n,m} + \dot{\xi}_{n,m}\,\Delta t, \tag{8}$$

$$\lambda \cdot \frac{\partial^2 T}{\partial x^2} + Q_\xi \dot{\xi} = \rho c \frac{\partial T}{\partial t},$$

$$T_{n+1,m} = T_{n,m} + \frac{\lambda}{\rho c}\frac{\Delta t}{\Delta x^2}\left(T_{n,m+1} - 2\,T_{n,m} + T_{n,m-1}\right) \tag{9}$$

$$+ \frac{\Delta t}{\rho c}\,C\,Q_{\max}\,\dot{\xi}_{n,m},$$

where $Q_{\max}$ (kJ/kg) is the total amount of heat and $C$ (kg/m$^3$) is the cement content per 1 m$^3$ volume. The iterative process ended with the convergence condition $\left|T_{n+1,m}^{(i+1)} - T_{n+1,m}^{(i)}\right|/T_r < \varepsilon$, where $T$ is the reference temperature. The iteration results were updated to the new step, and the boundary conditions were adopted each time according to the following formulations:

$$T_{n+1,1} = \left(\frac{\lambda_{\text{iz}}}{d_{\text{iz}}} T_{\text{env}} + \frac{\lambda}{\Delta x} T_{n+1,2}\right) \Big/ \left(\frac{\lambda_{\text{iz}}}{d_{\text{iz}}} + \frac{\lambda}{\Delta x}\right), \tag{10}$$

$$T_{n+1,m_s} = \left(\frac{\lambda_{\text{iz}}}{d_{\text{iz}}} T_{\text{env}} + \frac{\lambda}{\Delta x} T_{n+1,m_s-1}\right) \Big/ \left(\frac{\lambda_{\text{iz}}}{d_{\text{iz}}} + \frac{\lambda}{\Delta x}\right), \tag{11}$$

where $d_{\text{iz}}$ (m) is the thickness of the insulation, and $\lambda_{\text{iz}}$ (W/(m K)) is the insulation coefficient of thermal conductivity (Fig. 1). For the applied model, the validation process was successfully conducted based on literature data [28] and then used for the analysis of cases of concrete temperature evolution.

# 3 Materials and Methods of Investigation

## 3.1 Concrete Composition

In this study, six distinct concrete mixtures were meticulously produced under controlled laboratory conditions, incorporating diverse types of cement and aggregates (refer to Table 1 for details). The investigation encompassed two varieties of coarse aggregates, namely gravel and basalt, and three different cement types: Portland cement CEM I 42.5R, Portland composite cement CEM II/B-M (S-V) 42.5 N, which includes silica fly ash and granulated blast furnace, and blast furnace slag cement CEM III/A 42.5N—LH/HSR/NA. These cement types were sourced from the Polish Company Górażdze and adhered to specified requirements [32]. Table 2 provides the chemical compositions of these cement types, determined through X-ray Energy Dispersive Spectroscopy (EDS). Mixes dedicated to practical concrete structures were designed. The concrete mixtures were tailored to align with practical applications in concrete structures. Formulations were meticulously calculated to meet the criterion of compactness, ensuring that the sum of individual component volumes equaled the volume of the entire mixture (1 m³). The assumed densities for various materials were as follows: 3100 kg/m³ for cement, 1000 kg/m³ for water, 2650 kg/m³ for sand and gravel, and 3090 kg/m³ for basalt. A consistent water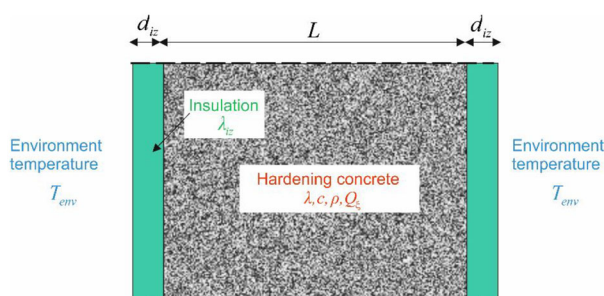–cement ratio ($w/c = 0.5$) was maintained across all considered mixtures. Theoretical densities were computed, resulting in 2419 kg/m³ for the concrete mix with gravel aggregate and 2619 kg/m³ for the mix with basalt aggregate. These meticulously designed mixtures aim to facilitate a comprehensive exploration of the impact of different cement and aggregate combinations on concrete properties.

## 3.2 Temperature Measurements in Concrete Cubes

To capture thermal data for 150 mm cubic specimens cured under room temperature conditions and those in insulation boxes, an original measurement system (Fig. 2) was employed. This system comprises a central unit and waterproof digital DS18B20-type temperature sensors. Utilizing a 1-wire bus, the thermocouple communicates with the central processor through a single data line. Each DS18B20 sensor possesses a unique 64-bit serial code, enabling multiple sensors to function on the same 1-wire bus. This design facilitates the use of a single microprocessor to control several thermocouples distributed over a considerable area. Operating within a temperature range of − 55 to 125 °C, with an accuracy of ± 0.5 °C, and requiring no calibration, the DS18B20s ensure the reliability of the recorded data. The high-precision temperature monitoring allows concrete temperature measurement at 20 points, operating on battery power for approximately 30 days. The data are sent to the server every hour via a GSM modem. Measurement points can be installed separately or using a prefabricated strip with multiple sensors arranged according to the project. The DS18B20 thermometer finds application not only in concrete temperature monitoring but also in systems within buildings, equipment, machinery, and various process monitoring and control systems.

The concrete cubes were cast in 150 mm polystyrene cubic moulds. For every mixture, six cubes were formed, three were dedicated to room conditions, and three were
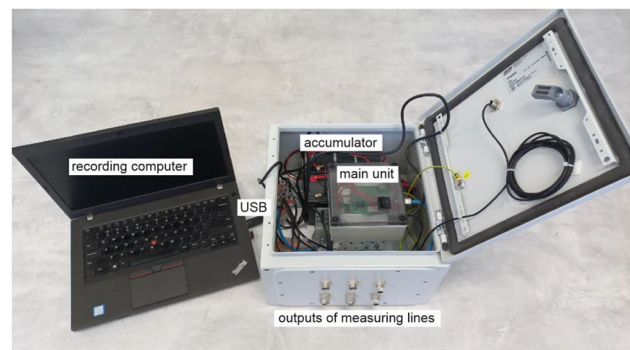


**Fig. 1** One-dimensional domain for the heat transfer



**Fig. 2** Temperature measurement system

**Table 1** Overview of mix proportions (kg/m$^3$)

| Mix | Cement | Water | Sand 0/2 | Gravel 2/8 | Gravel 8/16 | Basalt 2/8 | Basalt 8/16 |
|---|---|---|---|---|---|---|---|
| CEM I + gravel | 340 | 170 | 705 | 537 | 667 | – | – |
| CEM I + basalt | 340 | 170 | 705 | – | – | 626 | 778 |
| CEM II + gravel | 340 | 170 | 705 | 537 | 667 | – | – |
| CEM II + basalt | 340 | 170 | 705 | – | – | 626 | 778 |
| CEM III + gravel | 340 | 170 | 705 | 537 | 667 | – | – |
| CEM III + basalt | 340 | 170 | 705 | – | – | 626 | 778 |

**Table 2** Oxide composition of cements

| Cement type | CaO | SiO$_2$ | Al$_2$O$_3$ | Fe$_2$O$_3$ | SO$_3$ | MgO | K$_2$O | Others |
|---|---|---|---|---|---|---|---|---|
| CEM I | 61.3 | 13.7 | 7.3 | 9.9 | 4.7 | 0.8 | 2.1 | 0.2 |
| CEM II | 45.2 | 18.9 | 16.1 | 11.6 | 3.5 | 0.9 | 3.3 | 0.5 |
| CEM III | 50.7 | 24.1 | 11.3 | 5.6 | 4.5 | 2.3 | 1.2 | 0.3 |

placed in specially prepared styrofoam containers with a 100 mm thick insulation layer (Fig. 3). The boxes limited the heat exchange with the surroundings. Immediately after moulding, the temperature sensors were mounted in the cubic centre, and the concrete temperature changes were recorded for 7 days.

## 3.3 Adiabatic Calorimetry

The adiabatic method emerges as a suitable solution for accurately assessing the heating process within massive concrete structures. This approach is characterized by maintaining adiabatic conditions, thereby preventing heat exchange with the environment. Despite the inherent non-infinite conductivity of insulating materials, efforts are made to ensure that the room temperature closely matches (or is slightly lower by a maximum of 0.5 °C) the temperature of the specimen throughout the entire test.

The heat released by concrete during the hardening process under adiabatic conditions was measured according to the procedure specified in [22]. The adiabatic concrete calorimeter used in these studies (Fig. 4) was equipped with an external insulating enclosure, a calorimeter cell, two platinum PT 100 temperature sensors to measure the sample and cell temperatures, and a PC software. A fresh sample was cast into a 150 mm polystyrene cubic mould
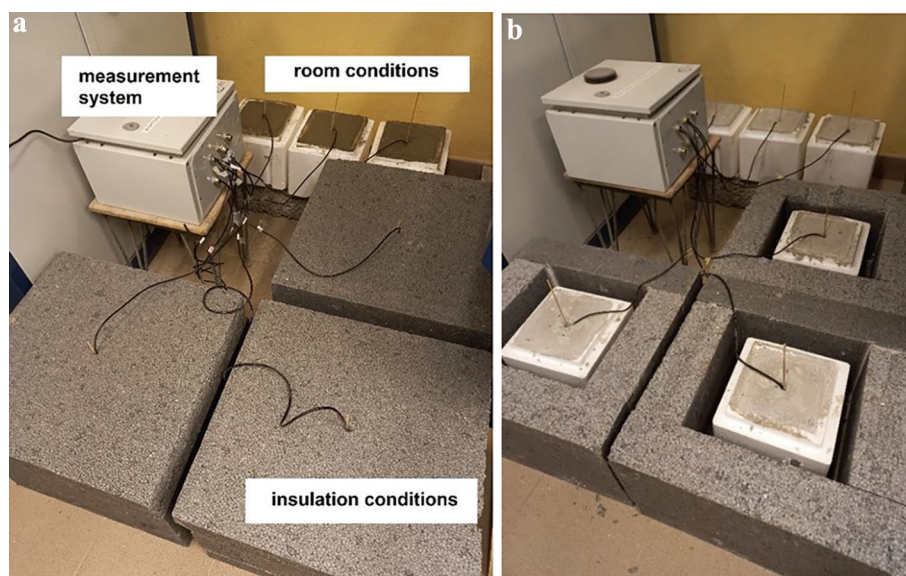


**Fig. 3** Concrete temperature measurements: **a** cubes after casting; **b** Cubes after 7 days
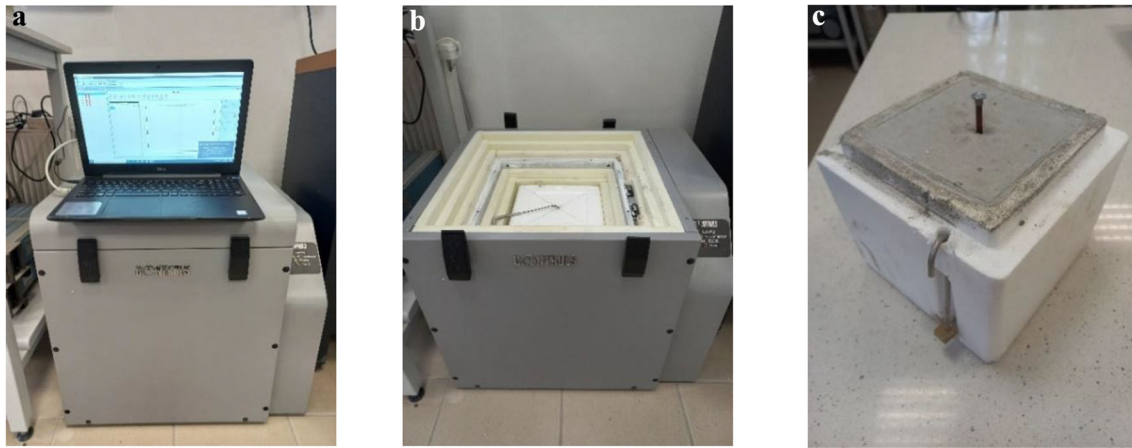
**Fig. 4** Adiabatic concrete calorimeter: **a** general view; **b** calorimeter cell; **c** 7-day cube

protected with a cover (according to [33] and [34]). The initial time (the time at which water was added to the cement and aggregate) and temperature of the concrete mix ($T_{con,0}$) were recorded. The masses of the container and concrete sample were also registered and input to the software. Subsequently, the hooks were fixed to the polystyrene mould for better handling, and a temperature probe tube was installed at the centre of the mould. To enhance thermal transmission, the sample temperature probe and the metallic edge of the test chamber were coated with a conductive paste [35].

Each test's duration was set to 168 h (7 days). The temperature changes measured over 24 h were consistently less than 1 °C, leading to the assumption that the bulk of the hydration reaction had occurred, and no significant further heat release was anticipated. Temperature measurements were performed using a PID closed-loop control system to ensure stable sample conditioning according to standard requirements. The temperatures of the concrete specimen ($T_{con}$) and calorimeter cell ($T_{cal}$) were recorded at 1 min intervals.

The temperature rise ($\Delta T_m$) of the concrete sample was calculated using the following equation:

$$\Delta T_m(t) = T_{con}(t) - T_{con,0}. \tag{12}$$

However, recognizing the practical limitations of achieving perfect adiabatic conditions, the intrinsic temperature rise ($\Delta T_c^*$) was computed using the formula:

$$\Delta T_c^*(t) = \left(1 + \frac{C_{cal}}{C_{con}}\right) \cdot (\Delta T_m(t) + \alpha \cdot t), \tag{13}$$

where $\alpha$ represents the adiabatic error, $C_{cal}$ represents the heat capacity of the calorimeter, and $C_{con}$ represents the total heat capacity of the concrete specimens. The value of $C_{con}$ is:

$$C_{con} = (c_c \cdot m_c + c_a \cdot m_a + c_w \cdot m_w), \tag{14}$$

where $c_c$, $c_a$, and $c_w$ are the specific heats of the cement, aggregate, and water, respectively. Similarly, $m_c$, $m_a$, and $m_w$ refer to the masses of the cement, aggregate, and water (in the sample), respectively. The following values were assumed for each calorimetric test: $c_c = c_a = 840\,(J/(kg\,k))$ and $c_w = 3760(J/(kg\,k))$. Finally, the cumulative development of the heat of hydration of the concrete was determined using Eq. (15):

$$Q(t) = \frac{(C_{con} + C_{cal}) \cdot \Delta T_c^*(t)}{m_c}. \tag{15}$$

### 3.4 Compressive Strength and Activation Energy

Destructive tests were undertaken to assess the impact of curing conditions on the mechanical properties of concrete. Following the completion of temperature measurements on day 7, the compressive strength of the young concrete was determined using an Advantest 9 C3000kN computer-controlled mechanical testing machine. Compression tests were conducted on concrete specimens in accordance with standard procedures [36], employing a constant loading rate of 0.5 MPa/s.

An essential parameter influencing the temperature variation of young concrete is the apparent activation energy, crucial for numerical calculations of temperature evolution and the maturity index of hardened concrete [37]. The annex of [38] presents three methods for determining the apparent activation energies. To specify the value of $E_a$, tests were performed on 50 mm mortar cubic specimens, prepared in accordance with requirements [38]. Each mortar shared the same water–cement ratio as the concrete, and the fine aggregate-to-cement ratio in the paste matched the coarse aggregate-to-cement ratio of the investigated
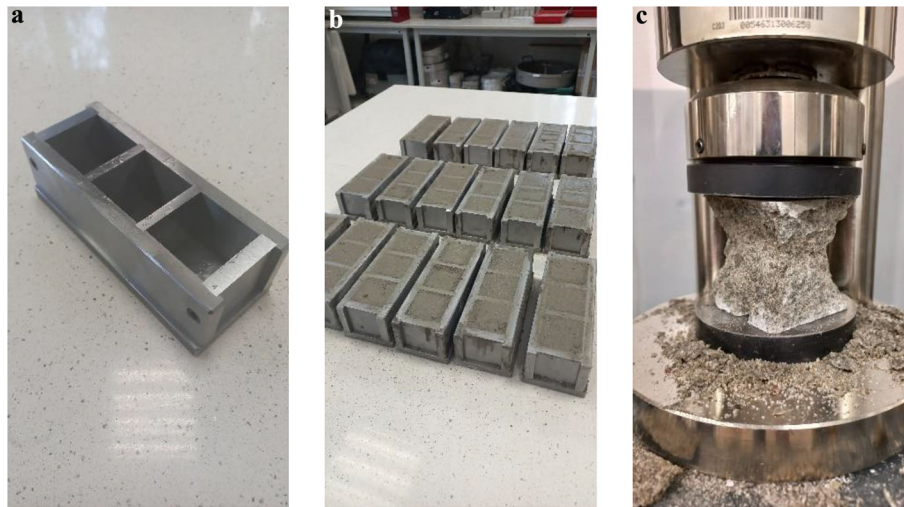
**Fig. 5** **a** 50 mm three-gang cube mould; **b** 54 fresh mortar samples; **c** compression test

concrete mix. Three types of mortar related to CEM I, II, and III were considered (Fig. 5). These samples (18 cubes per set) were molded using test method [39] and cured in water baths at specified temperatures: 10, 20, and 30 °C. Compressive strengths were tested after 1, 2, 5, 7, 14, and 28 days of mortar hardening.

According to [38], the determination of $E_a$ involves the calculation of the rate constants ($k-$values) for each mortar. The procedure described in point A1.1.8.1 [38] includes a nonlinear regression analysis of the strength-age data to define the rate constants by fitting the set of data with a hyperbolic equation:

$$S = S_u \cdot \frac{k \cdot (t - t_0)}{1 + k \cdot (t - t_0)}, \tag{16}$$

where $S$ is the compressive strength at time $t$, $S_u$ is the ultimate compressive strength, and $t_0$ represents the age at which strength development begins. The parameters $S_u$, $k$, and $t_0$ were determined using least-squares regression. Another function employed in these studies is the stretched exponential equation proposed in [40]:

$$S = S_u \cdot \exp\left(-\left(\frac{\tau}{t}\right)^{\beta}\right), \tag{17}$$

where $\beta$ is a shape constant, and $\tau$ represents a time constant.

## 4 Thermal History of Concrete Cubes

### 4.1 Room and Insulation Conditions

The temperature histories of concrete cubes subjected to room and insulation conditions are illustrated in Fig. 6. The recorded data demonstrated consistency, affirming the quality of thermal measurements. Concrete temperatures for samples cured under insulation conditions were notably higher than those cured under room conditions for all considered mixtures. The average initial temperatures varied from 19.5 °C for concrete with CEM I and gravel aggregate (Fig. 6a) to 22.4 °C for concrete with CEM II and gravel aggregate (Fig. 6c).

A comparison of the average temperature increases for the samples cured under two different conditions is depicted in Fig. 7. Under room temperature conditions, the temperature increase was not significant (Fig. 7a). As summarised in Table 3, the highest temperature increase was noted for concrete made from CEM II and basalt aggregate (5.90 °C) and the lowest for mixture with CEM I and basalt aggregate (2.25 °C). However, no visible relationship was observed between the thermal histories of the mixtures. This indicates that the volume of the concrete samples (3.375 dm$^3$) was too small to record clear temperature differences under ambient conditions. Additionally, the cubes were exposed to fluctuations and differences in environmental temperature which had an impact on the concrete temperature.

As shown in Fig. 6, the recorded temperatures were significantly higher for the concrete samples cured under insulation conditions. Styrofoam containers limited heat exchange, resulting in higher temperatures than those under room conditions. Despite the small volume of concrete, the influence of the type of cement and aggregate on the temperature increase in the concrete was distinctly noticeable (Fig. 7b, Table 3). The maximum value of temperature rise (17.0 °C) was reported for concrete with CEM I and gravel aggregate, while the lowest value of temperature increase (8.0 °C) was observed for mixture performed from CEM III and basalt aggregate (Fig. 7b, Table 3). Portland cement had the highest amount of
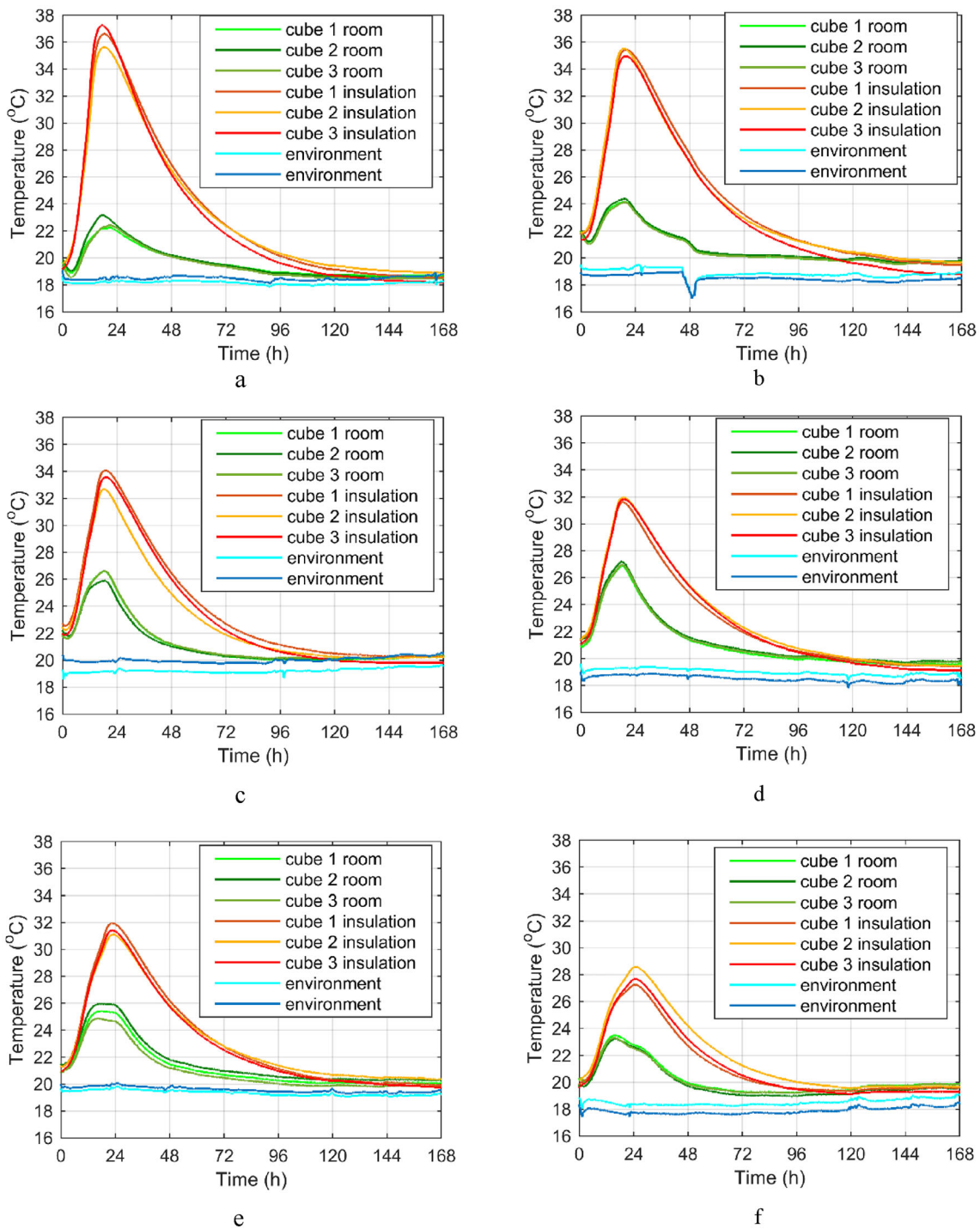
**Fig. 6** Temperature evolutions of concrete cubes curing in room and insulation conditions: **a** CEM I + gravel; **b** CEM I + basalt; **c** CEM II + gravel; **d** CEM II + basalt; **e** CEM III + gravel; **f** CEM III + basalt

clinker, whereas slag cement had the highest amount of nonclinker constituents. These results confirm that the substitution of clinker with mineral additives reduces the increase in temperature. It is worth noting that the aggregate type also affects the temperature development of young concrete. Under room temperature conditions, the temperature rise was not significant for any of the mixtures (Table 3). Thus, it is difficult to determine the effect of aggregate type on the increase in concrete temperature. However, under insulation conditions, a clear relationship was observed between the type of cement and aggregate. The use of basalt aggregates reduced the maximum
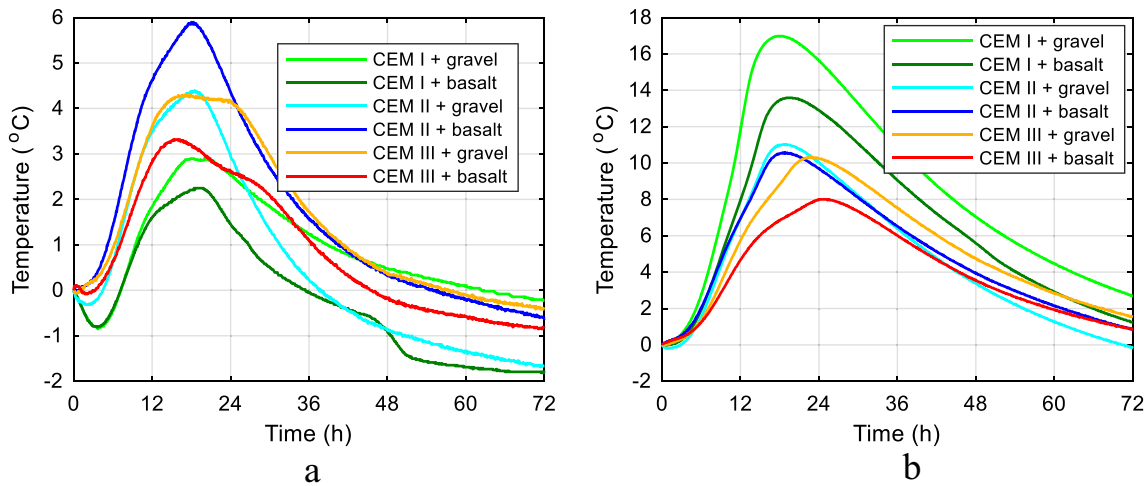
**Fig. 7** Average temperature increase of concrete cubes curing in: **a** room conditions and **b** insulation conditions

**Table 3** Maximum values of average temperature rise of concrete samples

| Mix | Temp rise—room conditions (°C) | Temp rise—insulation conditions (°C) |
|---|---|---|
| CEM I + gravel | 2.96 | 17.00 |
| CEM I + basalt | 2.25 | 13.58 |
| CEM II + gravel | 4.39 | 11.04 |
| CEM II + basalt | 5.90 | 10.58 |
| CEM III + gravel | 4.33 | 10.33 |
| CEM III + basalt | 3.32 | 8.00 |

temperature of concrete for all mixes, particularly for the mixture with Portland cement (by 20.1%, Table 3). The lowest impact of the aggregate type was observed in the case of Portland composite cement (CEM II). Among all the aggregates considered, the basalt aggregate had the highest thermal capacity and efficiently accumulated the thermal energy.

## 4.2 Adiabatic Conditions

The results of calorimetric tests on concrete samples cured under adiabatic conditions are presented in Figs. 8, 9. The summary of the essential values from conducted tests is shown in Table 4. The highest intrinsic temperature rise, reaching 47.3 °C, was recorded for concrete made of CEM I and gravel aggregate (Fig. 8). The presence of basalt aggregate decreased the maximum value of $\Delta T_c^*$ by

approximately 2.6 °C for a mixture with CEM I. In the case of CEM II, the maximum intrinsic temperature rise for gravel and basalt aggregate was 43.5 and 41.9 °C, respectively. The lowest value of $\Delta T_c^*$ was registered for concrete moulded from CEM III. After 168 h of hardening, the temperature rise was equal to 39.6 and 38.3 °C for gravel and basalt aggregate, respectively (Fig. 8, Table 4). The observed relationship between the considered mixtures is directly related to the clinker content in the cement composition. Portland cement (CEM I) consists of over 95% clinker, thus having the highest amount of calcium oxide, resulting in the most significant temperature rise. Lower temperatures were noted in concretes made of cement with non-clinker constituents. Additionally, the temperature of concrete with cement containing fly ash (CEM II/B-M (S-V) 42.5N) is greater than that of concrete with cement containing slag (CEM III/A 42.5N—LH/HSR/NA). The use of a mixture with slag cement and basalt aggregate allows for a significant reduction in concrete temperature, especially during the first 72 h of hardening. For example, at 40 h, the temperature difference between concrete made from CEM I with gravel aggregate and CEM III with basalt aggregate was 18 °C. Furthermore, the use of basalt aggregate reduces the temperature rise for each considered concrete (Fig. 8).

The adiabatic temperature increase was primarily due to the heat released from the binder used in the concrete. The average value of the maximum heat (after 7 days) generated by concrete with CEM I was 357.3 J/g, with CEM II it was 331.7 J/g, and with CEM III, it was 302.7 J/g (Fig. 9, Table 4). The use of slag cement reduced the maximum heat by 15.3% compared to Portland cement. In the initial phase of concrete hydration (up to 84 h), the heat evolved for samples with gravel aggregates was higher than that for basalt aggregates. In the final stage (168 h) of hydration,
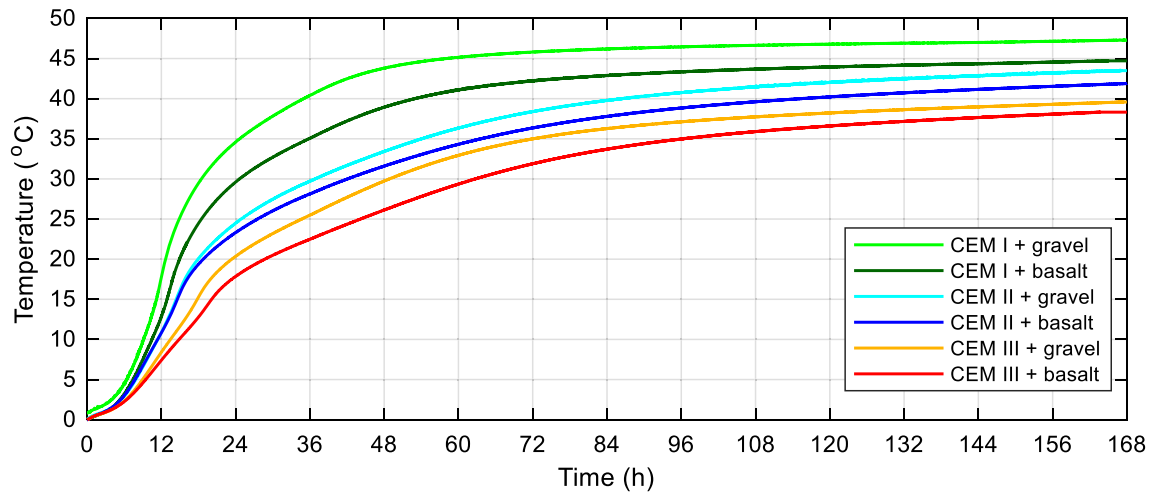
**Fig. 8** Evolution of intrinsic temperature rise $(\Delta T_c^*)$ of concrete under adiabatic conditions
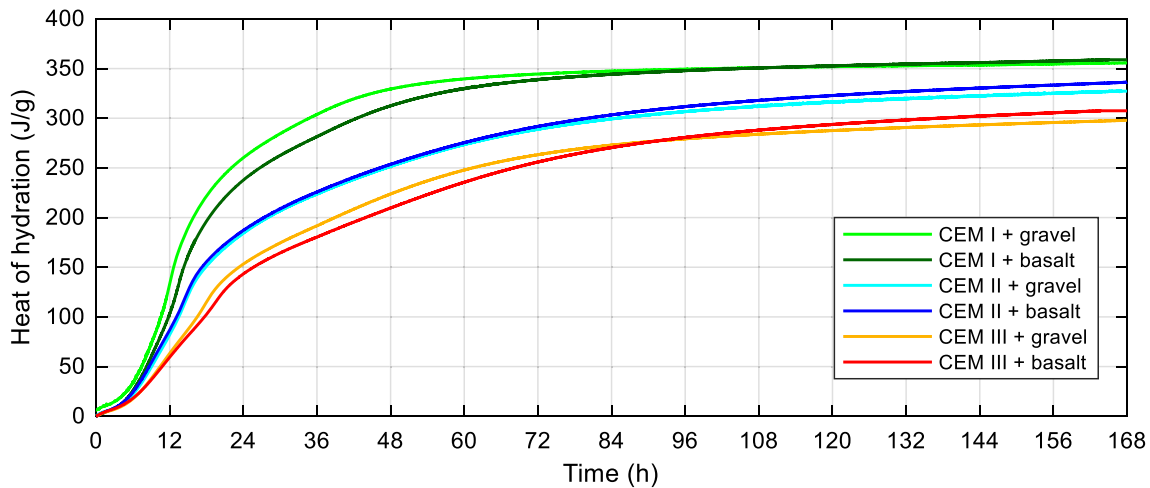


**Fig. 9** Heat of concrete hydration $(Q)$ under adiabatic conditions

**Table 4** Results of adiabatic tests

| Mix | Temperature rise | Heat | Peak of heat rate | |
|---|---|---|---|---|
| | max $\Delta T_c^*$ (°C) | $Q_{max}$ (J/g) | Time (h) | $dQ/dt$ (J/(g h)) |
| CEM I + gravel | 47.3 | 355.7 | 11.52 | 27.02 |
| CEM I + basalt | 44.7 | 358.9 | 12.97 | 22.52 |
| CEM II + gravel | 43.5 | 327.2 | 13.95 | 14.61 |
| CEM II + basalt | 41.9 | 336.2 | 14.02 | 14.81 |
| CEM III + gravel | 39.6 | 297.8 | 17.28 | 10.26 |
| CEM III + basalt | 38.3 | 307.5 | 19.00 | 8.64 |

the heat released for mixtures with basalt aggregates was slightly higher than that for mixtures with gravel aggregates. Adiabatic tests confirmed that basalt aggregate is characterized by a higher heat capacity than gravel aggregate and can accumulate thermal energy that is released in a later period.

The heat generation rates of concrete cured under adiabatic conditions are presented in Fig. 10. The initial period of heat evolution was very intense due to water absorption and surface dissolution of the cement grains. Subsequently, a dormant period was observed, and heat development decreased. Owing to the growth of the hydration product, the heat release increased steadily, reaching a maximum value of 27.02 J/g/h at 11.52 h for concrete with CEM I and gravel aggregate. The minimum value of the peak, equal to 8.64 J/g/h, was noticed at 19 h for concrete with CEM III and basalt aggregate (Fig. 10, Table 4). It is worth noting that the value of the maximum exothermic peak and its time of occurrence were prolonged in the presence of fly ash or slag compared to concrete with Portland cement. The addition of non-clinker distinctly retards the acceleratory period of cement hydration, as also
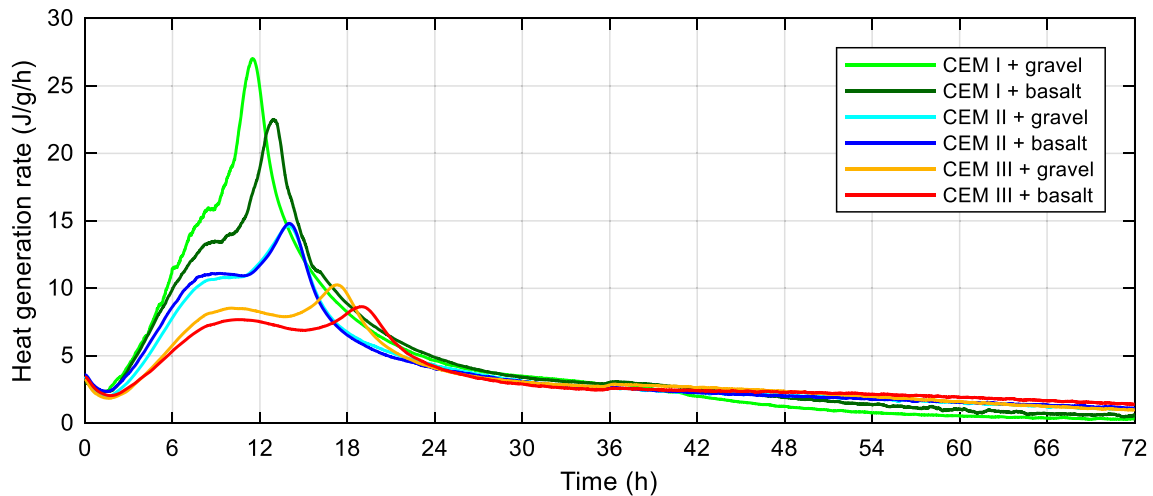
**Fig. 10** Heat generation rate of concrete under adiabatic conditions in the first 72 h

described in [41]. The slag contained in CEM III is a latent hydraulic material that mainly consists of an amorphous phase [41], decreasing the speed of the hydration reaction. CEM II contained slag and fly ash, which are pozzolanic materials. However, according to [42, 43], fly ash does not chemically react during the first 7 days; thus, the heat induced by the pozzolanic reaction occurs later. As demonstrated in Fig. 10, the use of basalt aggregate affected the reduction in the main hydration peak compared to the gravel aggregate. However, in the case of concrete with Portland composite cement (CEM II), the effect of the aggregate type on the rate of heat evolution was not observed. After approximately 3 d, the total heat evolved slowly, hydration products formed on the cement particles, and the entire process was diffusion-controlled [44].

# 5 Mechanical Properties

## 5.1 Compressive Strength of Concrete

Figure 11a depicts the results of the average compressive strength test on 150 mm concrete cubes cured under room and insulation conditions. The standard deviation values of the strength are also presented. Figure 11b illustrates the percentage of the 28-day characteristic compressive strength (37 MPa according to the C30/37 class) achieved after 7 days of hardening. For both figures (Fig. 11a and b), the results are presented from the highest to lowest values. Irrespective of the composition of the mixture, the concrete samples cured under insulation conditions exhibited the highest compressive strength compared to the room temperature samples. This indicates that the increased concrete temperature caused by the insulation effect enhances the
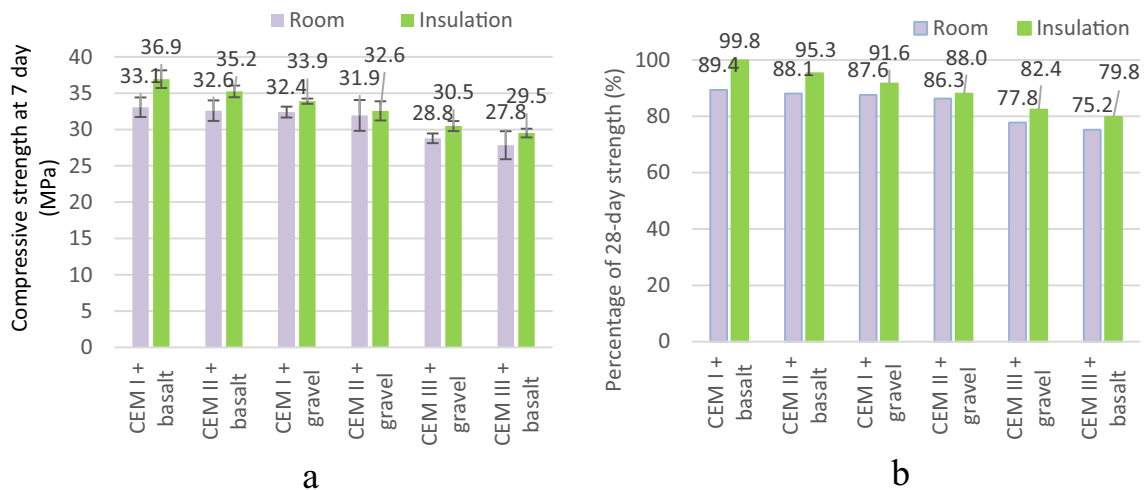


**Fig. 11** Compressive strength at 7 days for cubes cured at room and insulation conditions: **a** average values; **b** percentage of 28-day strength

7-day strength. Cubes made of Portland cement CEM I and basalt aggregate achieved the highest compressive strength, equal to 36.9 MPa and 33.1 MPa, which is 99.8% and 89.4% of the 28-day strength, for insulation and room conditions, respectively. The samples molded from CEM III and basalt aggregate reached the lowest strength, equal to 29.5 MPa and 27.8 MPa, which is 79.8% and 75.2% of the 28-day strength, for insulation and room conditions, respectively.

## 5.2 Apparent Activation Energy

The average mortar compressive strength data tested at 1, 2, 5, 7, 14, and 28 days, standard deviation of the strength, and exponential regression using Eq. (17) are shown in Fig. 12a–c. The standard deviation of the strength ranged from 0.1 to 4.0 MPa. As depicted in Fig. 12a–c, the highest compressive strength for each type of mortar was achieved for samples cured at 30 °C, and the lowest at 10 °C. At 5 days of hardening, in three considered temperatures (10, 20, 30 °C), the average compressive strength for mortar with CEM I was equal to 18.9, 24.7, 30.2 MPa, with CEM II 17.5, 21.0, 24.7 MPa, and with CEM III was equal to 16.2, 18.8, 28.0 MPa. The highest increase in early strength was noted for the paste with CEM I. In this case, a crossover effect was observed, i.e., after 28 days, the strength of the cubes cured at 10 °C was 1 MPa higher than cubes cured at 20 °C (Fig. 12a). After 28 days, in water baths at temperatures 10, 20, and 30 °C, the average strength was equal to 32.2, 31.2, 38.8 (CEM I), 31.6, 35.5, 39.2 (CEM II), and 36.9, 42.5, 53.5 (CEM III). It is worth noting that the cubes made using blast furnace cement exhibited the highest strength after 28 days of hardening (Fig. 12c).

The specified rate constants ($k$−values) indicate the possibility of drawing the natural logarithm of these values for the reciprocal of the temperature, expressed in Kelvin. The slope of the best-fit straight line indicates the apparent activation energy $E_a$, divided by the gas constant $R$. The results of the two considered functions (Eqs. (16) and (17)) and goodness of fit ($R^2$) are presented in detail in Tables 5 and 6. The rate constant $k$ achieved the highest value for the highest curing temperature i.e., 30 °C for every mortar. The largest value of the activation energy (33–34 kJ/mol) was observed for the paste produced using Portland cement CEM I (Fig. 12d). However, after considering Portland-composite cement CEM II (Fig. 12e) and blast furnace cement CEM III (Fig. 12f), the observed values were 30 and 22 kJ/mol, respectively. The relationship between the types of cement considered is in good agreement with the results obtained in [45].

## 6 Numerical Calculations

The thermochemical model described in Sect. 2 was used to calculate the temperature evolution in the concrete samples. Numerical calculations were performed using the FD method in the authors' program written in the MATLAB environment. A schematic diagram of the concrete thermal analysis conducted in this study is shown in Fig. 13.

The first stage focused on determining three model parameters: $\kappa/n_0$, $\overline{n}$, $A_0/\kappa$. The coefficient $\kappa/n_0$ influenced the reaction rate; $\overline{n}$ was responsible for the extreme temperature values, and $A_0/\kappa$ for the time of its occurrence. A detailed explanation of these parameters is presented in [24]. The measurement data obtained from the adiabatic tests of the concrete cubes allowed the calculation of the experimental chemical affinity according to Eq. (5). Based on regression analysis of the chemical affinity model Eq. (2) to the experimental values Eq. (5), three basic parameters were defined for each mixture.

In the next stage of analysis, the adiabatic temperature increase was calculated using the finite-difference method. The three identified parameters ($\kappa/n_0$, $\overline{n}$, and $A_0/\kappa$) were applied to the FDM code in MATLAB. This step allowed the comparison of the experimental and numerical adiabatic temperature rise curves and confirmed the correctness of all input data.

In the third stage of the research, nonadiabatic temperature curves were predicted through a combination of the results of an adiabatic temperature rise test and FD analysis. The heat transfer coefficient was defined and two model parameters ($\overline{n}$ and $A_0/\kappa$) were updated. Finally, the numerical and measured temperature histories of concrete cubes cured under insulation conditions were compared.

The constants used to solve the one-dimensional thermal problem are listed in Tables 7 and 8. The actual density of the concrete mix was lower than that of the mixture design owing to the presence of air voids. The following thermal parameters, $\lambda$, $\alpha_s$, $T_0$, and $T_{env}$, were only related to simulating nonadiabatic temperature evolution.

Initially, a thermal analysis of the mixture of CEM I and gravel aggregates was performed. The parameters $\kappa/n_0 = 1.1 \times 10^6$, $\overline{n} = 4.2$, and $A_0/\kappa = 10^{-2}$ were determined from the nonlinear regression of the chemical affinity using the least-squares method (Fig. 14a). The accuracy of the approximate data is described by a determination coefficient ($R^2$) of 0.9298. The appearance of a double peak in the calculated affinity shown in Fig. 14a is a feature of the $SO_3$ content of the Portland cement component of the binder. This characteristic is difficult to model unless the complexity of cement chemical composition is included in the model. Figure 14b compares the
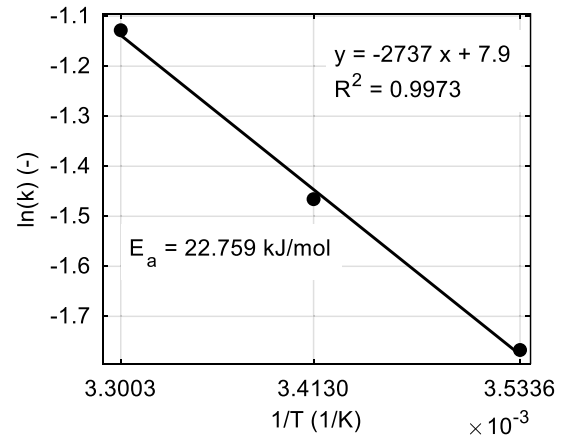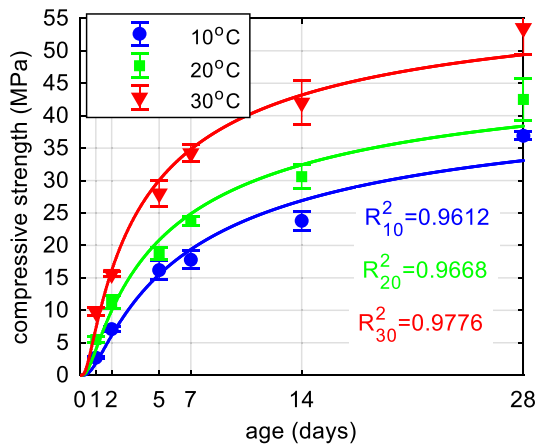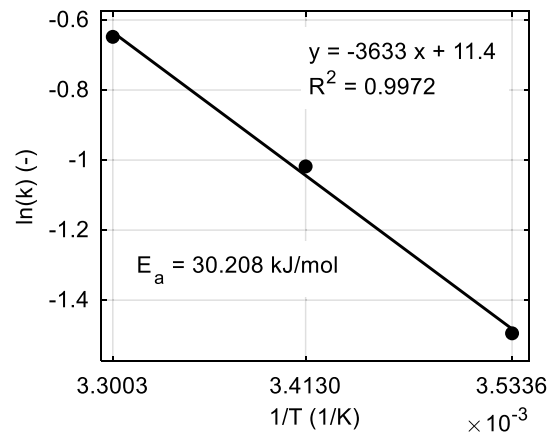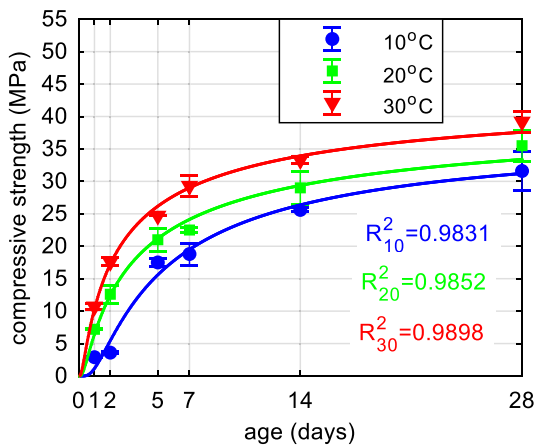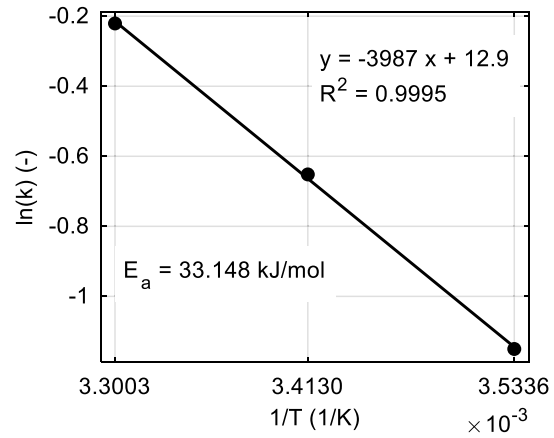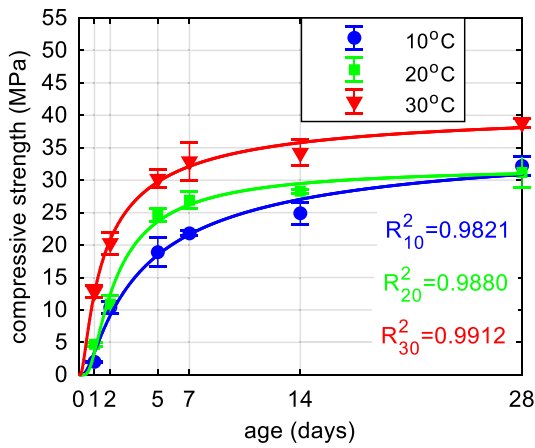
**Fig. 12** Strength–age relationship for mortar with: **a** CEM I, **b** CEM II, and **c** CEM III; linear regression for mortar with: **d** CEM I, **e** CEM II, and **f** CEM III

numerical predictions (black line) with the experimental data (red line) for the adiabatic temperature increase in the time domain. The adiabatic curve is plotted from 0 °C, which means that the temperature of concrete cured in the adiabatic calorimeter is approximately 20 °C higher than the temperature depicted in the graph. The difference between the measured and predicted temperature at 168 h

**Table 5** Analysis results for $E_a$ calculated using the hyperbolic function, Eq. (16)

| Mortar mixture identifier | Curing temperature (°C) | Nonlinear fit $S_u$ (MPa) | Straight-line fit $k$ (Day$^{-1}$) | Nonlinear fit $S_u$ (MPa) | Straight-line fit $k$ (Day$^{-1}$) | Nonlinear fit $S_u$ (MPa) | Straight-line fit $k$ (Day$^{-1}$) |
|---|---|---|---|---|---|---|---|
| CEM I | 10 | 34.62 | 0.273 | 0.687 | 0.9826 | 34.126 | 0.9999 |
| | 20 | 34.39 | 0.446 | 0.624 | 0.9783 | | |
| | 30 | 39.32 | 0.712 | 0.354 | 0.9890 | | |
| CEM II | 10 | 38.30 | 0.161 | 0.760 | 0.9787 | 30.237 | 0.9613 |
| | 20 | 37.78 | 0.289 | 0.518 | 0.9668 | | |
| | 30 | 41.11 | 0.375 | 0.201 | 0.9821 | | |
| CEM III | 10 | 45.27 | 0.112 | 0.560 | 0.9715 | 22.361 | 0.9875 |
| | 20 | 52.36 | 0.165 | 0.430 | 0.9348 | | |
| | 30 | 59.08 | 0.210 | 0.194 | 0.9864 | | |

**Table 6** Analysis results for $E_a$ calculated using the exponential function, Eq. (17)

| Mortar mixture identifier | Curing temperature (°C) | Nonlinear fit $S_u$ (MPa) | Straight-line fit $k = 1/\tau$ (Day$^{-1}$) | Nonlinear fit $S_u$ (MPa) | Straight-line fit $k = 1/\tau$ (Day$^{-1}$) | Nonlinear fit $S_u$ (MPa) | Straight-line fit $k = 1/\tau$ (Day$^{-1}$) |
|---|---|---|---|---|---|---|---|
| CEM I | 10 | 37.50 | 0.317 | 0.751 | 0.9821 | 33.148 | 0.9995 |
| | 20 | 32.18 | 0.521 | 1.225 | 0.9880 | | |
| | 30 | 41.49 | 0.802 | 0.791 | 0.9912 | | |
| CEM II | 10 | 38.66 | 0.224 | 0.839 | 0.9831 | 30.208 | 0.9972 |
| | 20 | 42.30 | 0.361 | 0.622 | 0.9852 | | |
| | 30 | 45.60 | 0.523 | 0.612 | 0.9989 | | |
| CEM III | 10 | 47.10 | 0.171 | 0.665 | 0.9612 | 22.759 | 0.9973 |
| | 20 | 51.76 | 0.231 | 0.647 | 0.9668 | | |
| | 30 | 61.78 | 0.324 | 0.680 | 0.9776 | | |

is equal to 0.58 °C. The modelled temperature evolution was in good agreement with the measurements.

The same procedure was adopted for six considered concrete mixes. The prediction results of the selected concrete i.e., concrete with CEM II + basalt and CEM III + gravel are presented in Figs. 15 and 16, respectively. In these cases, the differences between the registered and estimated temperatures at 168 h were 2.16 °C (Fig. 15b) and 1.81 °C (Fig. 16b), respectively. The parameters, $\kappa/n_0$, $\bar{n}$, and $A_0/\kappa$, and the determination coefficients for all mixes cured in adiabatic conditions are summarized in Table 9. It can be stated that the coefficient $\kappa/n_0$ that affects the reaction rate is the highest for concrete made from CEM I and gravel aggregate. Its value drops from 1.1 × 10$^6$ to 8.5 × 10$^3$ for concrete with CEM III and basalt aggregate. The observed relation is appropriate to the heat generation rate shown in Fig. 10. The linear relationship between $\kappa/n_0$ and peak value of heat ($dQ/dt$, Table 4) was

noted and written using the formula: $\kappa/n_0 = 64996 \cdot (dQ/dt) - 621835621835$ (the determination coefficient $R^2$ equals 0.9828). In the case of $\bar{n}$, the achieved values are not directly related to the extreme temperatures recorded in the adiabatic test (Fig. 8). This parameter varies from 4.2 for concrete with Portland cement and gravel aggregate to 5.0 for Portland composite cement with basalt aggregate. The coefficient $A_0/\kappa$ is responsible for the occurrence of temperature peak and is constant ($A_0/\kappa = 10^{-2}$) for all considered mixtures tested in the adiabatic calorimeter. It can be summarized that the prediction results of all concrete correspond with their measurements.

Considering the aforementioned results, numerical simulations of the temperature evolution of concrete cubes under insulation conditions were carried out. The implementation of the model parameters listed in Table 9 did not provide correct results. As demonstrated in Fig. 17a, the predicted temperature is higher than the measured one;

thus, the coefficients $\bar{n}$ and $A_0/\kappa$ were updated. It was assumed that the parameter $\kappa/n_0$ remained unchanged. The coefficient $A_0/\kappa$ controls the time of temperature peak occurrence. In adiabatic conditions, the temperature rises immediately, but in the non-adiabatic approach the temperature increase is delayed; therefore, instead of $10^{-2}$, the value of $10^{-4}$ was adopted. The main modification was related to $\bar{n}$. The value of this factor defined in nonadiabatic conditions increased in relation to the adiabatic conditions for each concrete mixture. The linear relationship between considered parameters was observed, and written by the formula: $\bar{n}_{semi-adia} = 2.25 \cdot \bar{n}_{adia} - 3.15$ (the determination coefficient $R^2$ equals 0.9693).

Table 10 lists the model parameters for all considered mixes, cured in insulation conditions. The parameter $\bar{n}$ is higher for mixes with basalt aggregate, and the highest values are taken for mix with Portland composite cement (Table 10). Figures 17, 18, 19 provide a comparison of the experimental and model nonadiabatic temperature rise curves for concrete with CEM I + gravel, CEM II + basalt, and CEM III + gravel. Additionally, the maps of concrete temperature distribution in space and time domains are illustrated in Fig. 20. The higher temperature difference between the core of the sample and the surface layer was noted in the case of CEM I + gravel in comparison to CEM II + basalt, i.e. 0.67 and 0.47 °C, respectively. To quantitatively compare the results of measurement and FDM analysis, the least square method was used. By adjusting the factors of $\bar{n}$ and $A_0/\kappa$, a good agreement is achieved between the numerical and experimental results. These results suggest that the model could be applied to predict the nonadiabatic response of a wide variety of concrete. It means that the proposed solution presents the possibility of evaluation of the temperature development of cast-in-place concrete.

# 7 Conclusions

The completed studies present valuable insights into the heat release characteristics of concrete under different curing conditions, ensuring a reliable comparison due to the consistent use of 150 mm cubes commonly employed in engineering practice. Notably, room conditions were found unsuitable for accurate thermal predictions, particularly due to the limited volume of concrete samples. Recommendations discourage this approach for numerical analysis and discourage its future use by researchers. Insulation conditions and adiabatic curing methods, however, proved effective in revealing key relationships between temperature rise and concrete type. Maximum temperature rises were observed for Portland cement concrete with gravel aggregate (17 °C and 47.3 °C,
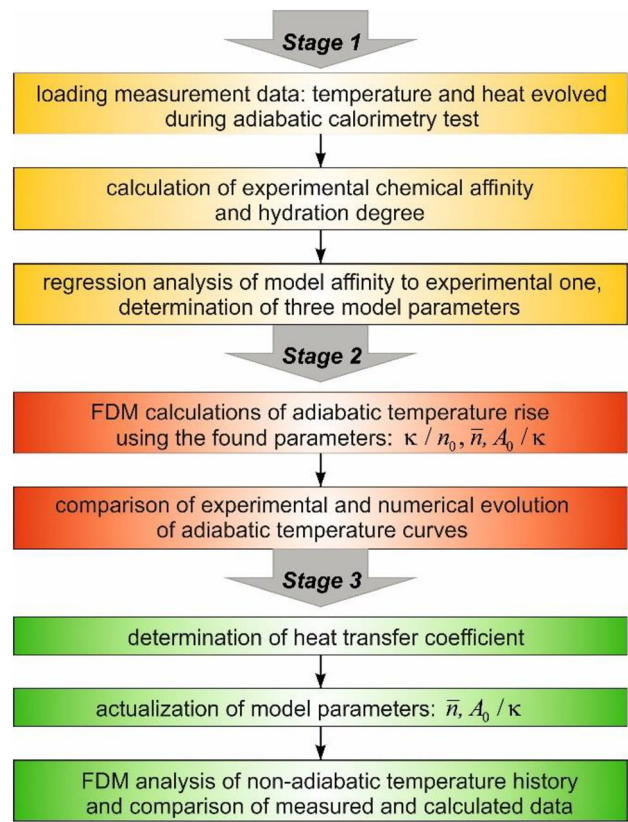


**Fig. 13** Scheme of numerical calculations of concrete temperature distribution

**Table 7** Constant thermophysical properties for all considered concretes

| C (kg/m$^3$) | w/c (–) | $\xi_{max}$ (−) | c (kJ/(kg K)) | $\lambda$ (W/(m K)) | $\alpha_s$ (W/(m$^2$ K)) |
|---|---|---|---|---|---|
| 340 | 0.5 | 0.7428 | 0.84 | 2.0 | 1.9 |

**Table 8** Input data for numerical analysis

| Mix | $\rho$ (kg/m$^3$) | $Q_{max}$ (kJ/kg) | $E_a/R$ (K) | $T_{env}$ (°C) | $T_0$ (°C) |
|---|---|---|---|---|---|
| CEM I + gravel | 2330 | 355.7 | 3987 | 18.0 | 19.5 |
| CEM I + basalt | 2480 | 358.9 | 3987 | 18.8 | 21.7 |
| CEM II + gravel | 2330 | 327.2 | 3633 | 19.3 | 22.4 |
| CEM II + basalt | 2480 | 336.2 | 3633 | 18.8 | 21.2 |
| CEM III + gravel | 2330 | 297.8 | 2737 | 19.5 | 21.2 |
| CEM III + basalt | 2480 | 307.5 | 2737 | 18.5 | 19.8 |

respectively), while mixtures incorporating blast furnace slag cement and basalt aggregate exhibited the lowest temperature increases (8.0 °C and 38.3 °C, respectively).
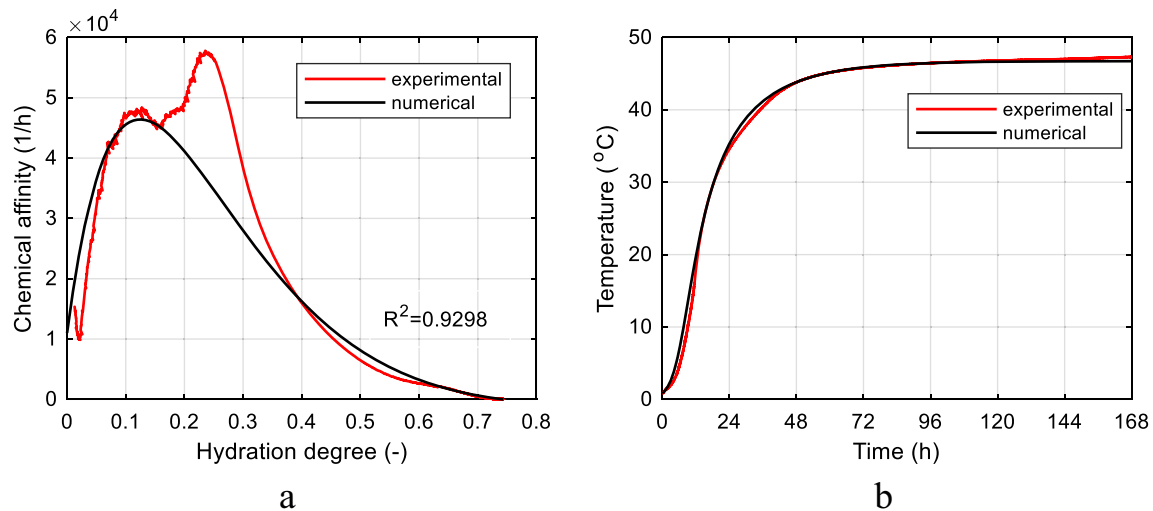
**Fig. 14** Comparison between the experimental and numerical results of mixture with CEM I and gravel: **a** approximation of chemical affinity vs. hydration degree; **b** temperature evolution in adiabatic conditions
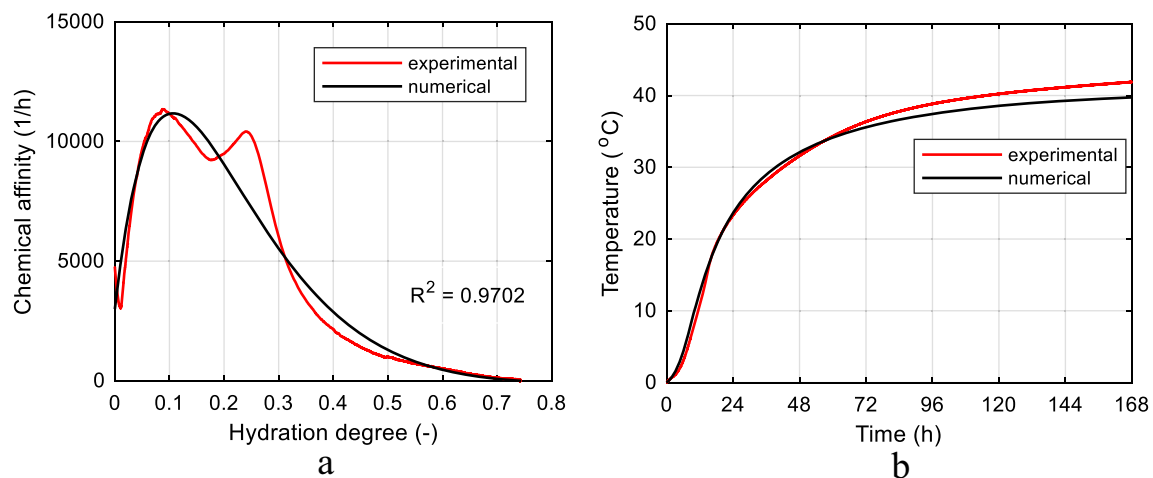


**Fig. 15** Comparison of experimental and numerical results of mixture with CEM II and basalt: **a** approximation of chemical affinity vs. hydration degree; **b** temperature evolution in adiabatic conditions

This relationship directly correlates with the clinker content and the highest amount of CaO in Portland cement composition. The substitution of clinker with slag, ash, or other mineral additives consistently reduced temperature increases. Additionally, basalt aggregate, with its higher heat capacity and ability to accumulate thermal energy, demonstrated effectiveness in reducing temperature rise for all considered concrete mixtures. Practical recommendations for concrete applications emerged from the findings. For structures requiring minimized heat release, such as massive foundations, a mixture of CEM III and basalt is recommended, significantly lowering maximum concrete temperature and delaying its occurrence. Conversely, for concreting bridge girders where time and strength gain are critical, a mixture of CEM I and basalt is suggested to

accelerate the hydration reaction and improve the building process.

The studies also delved into mechanical properties, highlighting that concrete cubes cured under insulation conditions exhibited the highest 7-day compressive strength compared to those cured in room conditions. This was attributed to a slower drying process and higher concrete temperature in insulation conditions, contributing to increased early-age compressive strength. Notably, cubes made of Portland cement and basalt aggregate achieved the highest strength, while those with blast furnace slag cement and basalt aggregate exhibited the lowest early-age strength. The apparent activation energy, determined using 50-mm mortar cubes, varied with the type of cement: 33.1 kJ/mol for CEM I, 30.2 kJ/mol for CEM II, and 22.8 kJ/mol for CEM III. This method is recommended for
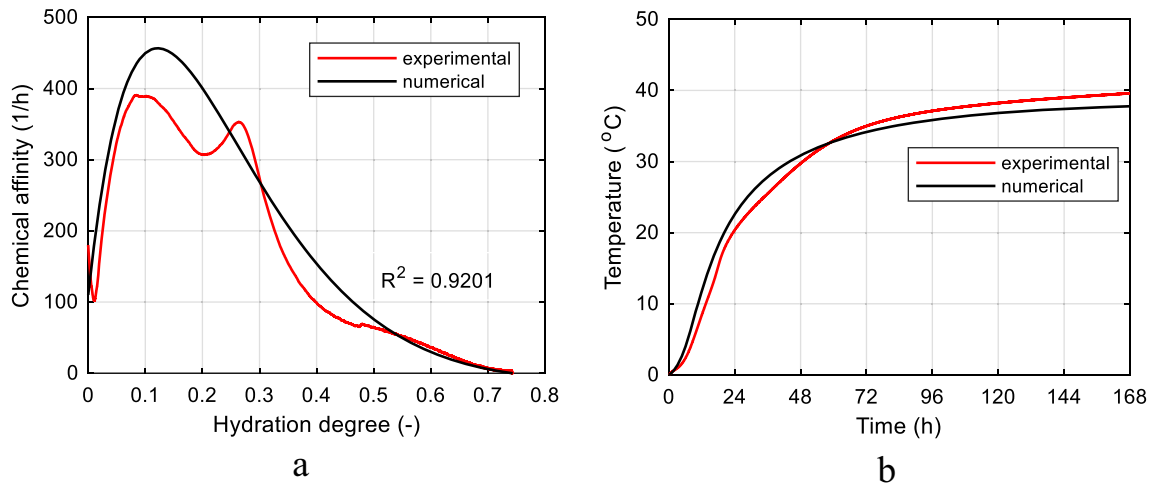
**Fig. 16** Comparison of experimental and numerical results of mixture with CEM III and gravel: **a** approximation of chemical affinity vs. hydration degree; **b** temperature evolution in adiabatic conditions

**Table 9** Model parameters for adiabatic tests

| Mix | $\kappa/n_0$ (1/h) | $\overline{n}$ (−) | $A_0/\kappa$ (−) | $R^2$ (−) |
|---|---|---|---|---|
| CEM I + gravel | $1.1 \times 10^6$ | 4.2 | $10^{-2}$ | 0.9298 |
| CEM I + basalt | $9.3 \times 10^5$ | 4.3 | $10^{-2}$ | 0.9485 |
| CEM II + gravel | $2.8 \times 10^5$ | 4.8 | $10^{-2}$ | 0.9669 |
| CEM II + basalt | $3.0 \times 10^5$ | 5.0 | $10^{-2}$ | 0.9702 |
| CEM III + gravel | $1.1 \times 10^4$ | 4.3 | $10^{-2}$ | 0.9201 |
| CEM III + basalt | $8.5 \times 10^3$ | 4.6 | $10^{-2}$ | 0.9696 |

**Table 10** Model parameters for non-adiabatic tests

| Mix | $\kappa/n_0$ (1/h) | $\overline{n}$ (−) | $A_0/\kappa$ (−) |
|---|---|---|---|
| CEM I + gravel | $1.1 \times 10^6$ | 6.1 | $10^{-4}$ |
| CEM I + basalt | $9.3 \times 10^5$ | 6.6 | $10^{-4}$ |
| CEM II + gravel | $2.8 \times 10^5$ | 7.5 | $10^{-4}$ |
| CEM II + basalt | $3.0 \times 10^5$ | 8.1 | $10^{-4}$ |
| CEM III + gravel | $1.1 \times 10^4$ | 6.6 | $10^{-4}$ |
| CEM III + basalt | $8.5 \times 10^3$ | 7.3 | $10^{-4}$ |
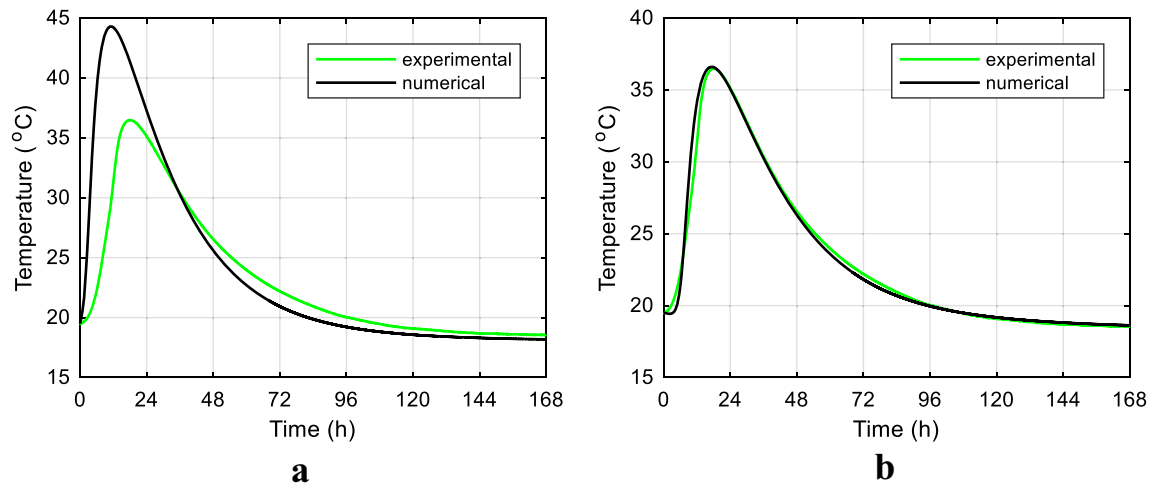


**Fig. 17** Comparison of experimental and numerical temperature evolution in insulation conditions of mixture with CEM I and gravel aggregate: **a** basic model parameters; **b** modified model parameters

determining activation energy due to its applicability and relevance.

The numerical analysis of the data obtained from the adiabatic temperature rise test allowed for the successful identification of model parameters, that is, $\kappa/n_0$, $\overline{n}$, and
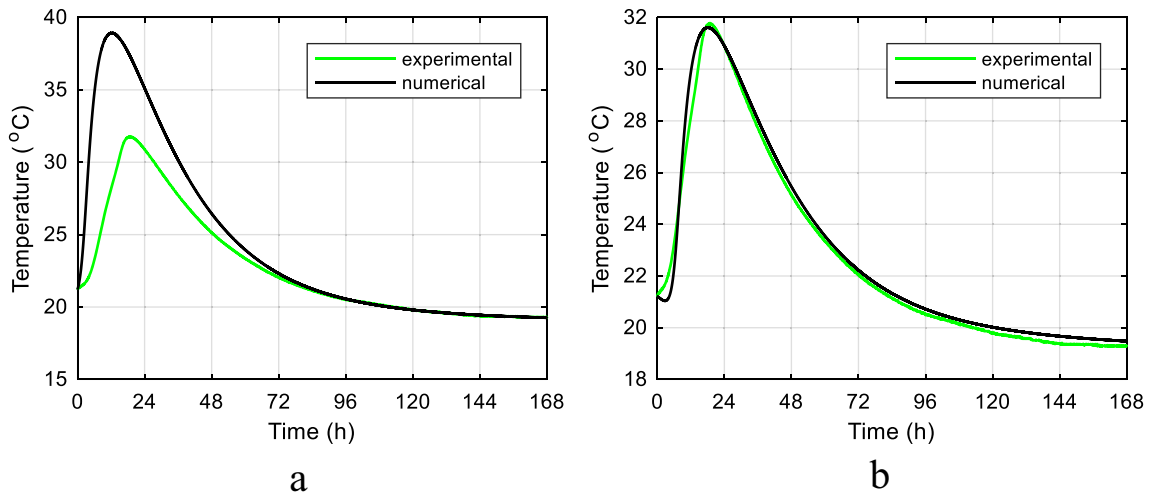
**Fig. 18** Comparison of experimental and numerical temperature evolution in insulation conditions of mixture with CEM II and basalt aggregate: **a** basic model parameters; **b** modified model parameters
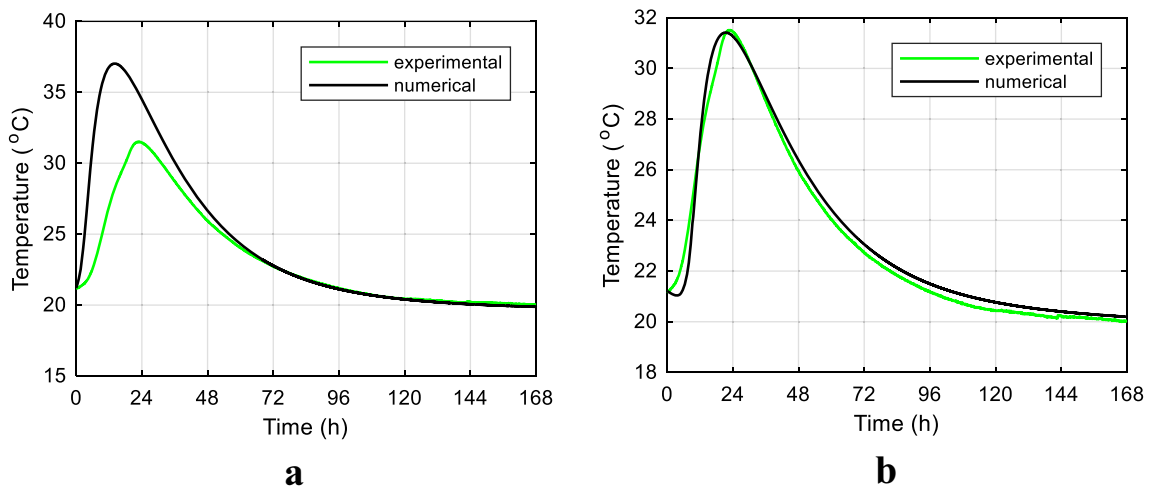


**Fig. 19** Comparison of experimental and numerical temperature evolution in insulation conditions of mixture with CEM III and gravel aggregate: **a** basic model parameters; **b** modified model parameters
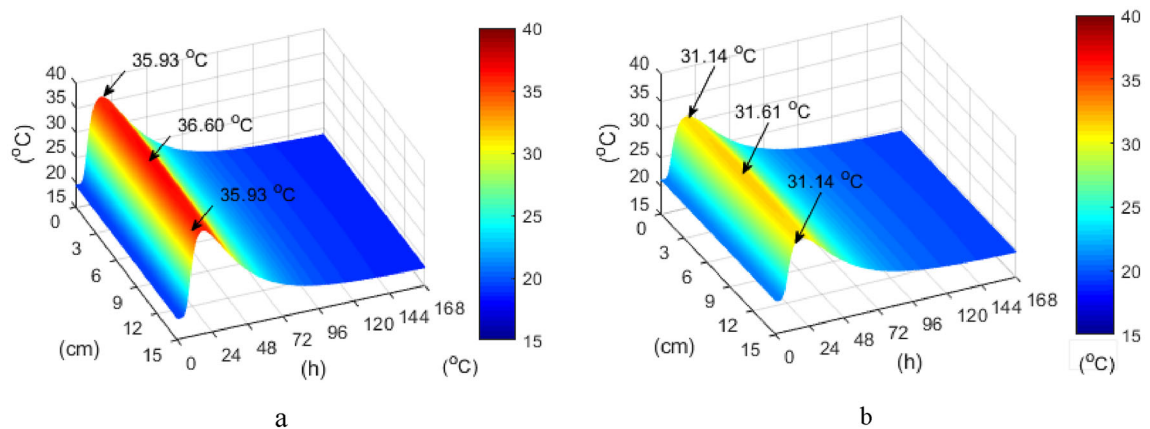


**Fig. 20** 1D maps of numerical temperature evolution in insulation conditions of mixture with: **a** CEM I and gravel aggregate; **b** CEM II and basalt aggregate

$A_0/\kappa$. These factors are crucial for the prediction of temperature development under nonadiabatic conditions using direct adiabatic tests. According to the input model parameter study for the FDM thermal analysis aimed at replicating the nonadiabatic temperature rise test, the critical parameters of the thermal properties are $\overline{n}$ and $A_0/\kappa$, because the coefficient of $\kappa/n_0$ is constant for both conditions. Finally, comparisons of the temperature evolution over time in the adiabatic and nonadiabatic tests confirmed that the model prediction was in good agreement with the measurements. The proposed solution could be successfully applied to predict the temperature increase in cast-in-place concrete. Such knowledge can be a complementary material for engineers interested in the construction control process, as well as for increasing the quality and durability of concrete structures.

**Data Availability** Data will be made available on request.

## Declarations

**Conflict of interest** The authors have not disclosed any conflict of interests.

**Ethical Approval** The authors state that the research was conducted according to ethical standards. This article does not contain any studies with human participants or animals performed by any of the authors.

## References

1. CEN, EN 13670 Execution of concrete structures. European Standards, European Committee for Standardization: Brussels, Belgium
2. An GH, Park JM, Cha SL, Kim JK (2016) Development of a portable device and compensation method for the prediction of the adiabatic temperature rise of concrete. Constr Build Mater 102:640–647. https://doi.org/10.1016/j.conbuildmat.2015.10.143
3. Lim CK, Kim JK, Seo TS (2016) Prediction of concrete adiabatic temperature rise characteristic by semi-adiabatic temperature rise test and FEM analysis. Constr Build Mater 125:679–689. https://doi.org/10.1016/j.conbuildmat.2016.08.072
4. Schackow A, Effting C, Gomes IR, Patruni IZ, Vicenzi F, Kramel C (2016) Temperature variation in concrete samples due to cement hydration. Appl Therm Eng 103:1362–1369. https://doi.org/10.1016/j.applthermaleng.2016.05.048
5. Ding J, Chen S (2013) Simulation and feedback analysis of the temperature field in massive concrete structures containing cooling pipes. Appl Therm Eng 61:554–562. https://doi.org/10.1016/j.applthermaleng.2013.08.029
6. Zou X, Chao A, Tian Y, Wu N, Zhang H, Yu TY, Wang X (2012) An experimental study on the concrete hydration process using Fabry-Perot fiber optic temperature sensors. Measurement 45:1077–1082. https://doi.org/10.1016/j.measurement.2012.01.034
7. Liang Z, Zhao Ch, Zhou H, Liu Q, Zhou Y (2019) Error correction of temperature measurement data obtained from an embedded bifilar optical fiber network in concrete dams. Measurement 148:106903. https://doi.org/10.1016/j.measurement.2019.106903
8. Liao W, Zhuang Y, Zeng CH, Deng W, Huang J, Ma H (2020) Fiber optic sensors enabled monitoring of thermal curling of concrete pavement slab: temperature, strain and inclination. Measurement 165:108203. https://doi.org/10.1016/j.measurement.2020.108203
9. Frølich L, Wadsö L, Sandberg P (2016) Using isothermal calorimetry to predict one day mortar strengths. Cem Concr Res 88:108–113. https://doi.org/10.1016/j.cemconres.2016.06.009
10. Linderoth O, Wadsö L, Jansen D (2021) Long-term cement hydration studies with isothermal calorimetry. Cem Concr Res 141:106344. https://doi.org/10.1016/j.cemconres.2020.106344
11. MacLeod AJN, Collins FG, Duan W (2021) Effects of carbon nanotubes on the early-age hydration kinetics of Portland cement using isothermal calorimetry. Cem Concr Compos 119:103994. https://doi.org/10.1016/j.cemconcomp.2021.103994
12. Hernandez-Bautista E, Bentz DP, Sandoval-Torres S, Cano-Barrita PFJ (2016) Numerical simulation of heat and mass transport during hydration of Portland cement mortar in semi-adiabatic and steam curing conditions. Cem Concr Compos 69:38–48. https://doi.org/10.1016/j.cemconcomp.2015.10.014
13. RILEM TC 119-TCE: Avoidance of thermal cracking in concrete at early ages (1997) Materials and structures. 30:451–464.
14. Ng I, Ng P, Kwan A (2009) Effects of cement and water contents on adiabatic temperature rise of concrete. ACI Mater J 106(1):42–49. https://doi.org/10.14359/5631
15. Ng P, Ng I, Kwan A (2008) Heat loss compensation in semi-adiabatic curing test of concrete. ACI Mater J 105(1):52–61. https://doi.org/10.14359/19207
16. Costa U (1979) A simplified model of adiabatic calorimeter. Il Cemento 76:75–92
17. Jeong DJ, Kim T, Ryu JH, Kim JH (2016) Analytical model to parameterize the adiabatic temperature rise of concrete. Cem Concr Compos 69:38–48. https://doi.org/10.1016/j.cemconcomp.2015.10.014

18. da Silva WRL, Šmilauer V, Stemberk P (2015) Upscaling semi-adiabatic measurements for simulating temperature evolution of mass concrete structures. Mater Struct 48(4):1031–1041. https://doi.org/10.1617/S11527-013-0213-3

19. Xu Q, Wang K, Medina C, Engquist B (2015) A mathematical model to predict adiabatic temperatures from isothermal heat evolutions with validation for cementitious materials. Int J Heat Mass Transf 89:333–338. https://doi.org/10.1016/j.ijheatmasstransfer.2015.05.035

20. Ramu YK, Akhtar I, Santhanam M (2016) Use of adiabatic calorimetry for performance assessment of concretes. Adv Cem Res 28(8):485–493. https://doi.org/10.1680/jadcr.15.00097

21. Lin Y, Chen HL (2015) Thermal analysis and adiabatic calorimetry for early-age concrete members. J Therm Anal Calorim 122:937–945. https://doi.org/10.1007/s10973-015-4843-2

22. CEN, EN 12390-15. Testing hardened concrete—Part 15: adiabatic method for the determination of heat released by concrete during its hardening process; European Standards, European Committee for Standardization: Brussels, Belgium

23. Kuryłowicz-Cudowska A, Wilde K, Chróścielewski J (2020) Prediction of cast-in-place concrete strength of the extradosed bridge deck based on temperature monitoring and numerical simulations. Constr Build Mater 254:119224. https://doi.org/10.1016/j.conbuildmat.2020.119224

24. Kuryłowicz-Cudowska A (2019) Determination of thermophysical parameters involved in the numerical model to predict the temperature field of cast-in-place concrete bridge deck. Materials 12:3089. https://doi.org/10.3390/ma12193089

25. Kuryłowicz-Cudowska A, Wilde K (2022) FEM and experimental investigations of concrete temperature field in the massive stemwall of the bridge abutment. Constr Build Mater 347:128565. https://doi.org/10.1016/j.conbuildmat.2022.128565

26. Zhou W, Qi T, Liu X, Yang S, Feng C (2019) A meso-scale analysis of the hygro-thermo-chemical characteristics of early-age concrete. J Heat Mass Transf 129:690–706. https://doi.org/10.1016/j.ijheatmasstransfer.2018.10.001

27. Zhao H, Jiang K, Yang R, Tang Y, Liu J (2020) Experimental and theoretical analysis on coupled effect of hydration, temperature and humidity in early-age cement-based materials. J Heat Mass Transf 146:118784. https://doi.org/10.1016/j.ijheatmasstransfer.2019.118784

28. Cervera M, Faria R, Oliver J, Prato T (2002) Numerical modelling of concrete curing, regarding hydration and temperature phenomena. Comput Struct 80:1511–1521. https://doi.org/10.1016/S0045-7949(02)00104-9

29. Bažant ZP, Thonguthai W (1978) Pore pressure and drying of concrete at high temperature. J Eng Mech Div 104(5):1059–1079

30. Majorana CE, Salomoni V, Schrefler BA (1998) Hygrothermal and mechanical model of concrete at high temperature. Mater Struct 31(6):378–386

31. Pantazopoulo SJ, Mills RH (1995) Microstructural aspects of the mechanical response of plain concrete. ACI Mater J 92(6):605–616

32. CEN, EN 197-1. Cement—Part 1: composition, specifications and conformity criteria for common cements; European Standards, European Committee for Standardization: Brussels, Belgium

33. CEN, EN 12350-1. Testing fresh concrete—Part 1: Sampling and common apparatus; European Standards, European Committee for Standardization: Brussels, Belgium

34. CEN, EN 12390-2. Testing hardened concrete—Part 2: making and curing specimens for strength tests; European Standards, European Committee for Standardization: Brussels, Belgium

35. Adiabatic Concrete Calorimeter 54-C2010/A, Instruction manual, Controls Group. (2017) 1–68

36. CEN, EN 12390-3. Testing hardened concrete. Part 3: compressive strength of test specimens; European Standards, European Committee for Standardization: Brussels, Belgium

37. Kuryłowicz-Cudowska A, Haustein E (2021) Isothermal calorimetry and compressive strength tests of mortar specimens for determination of apparent activation energy. J Mater Civ Eng 33:1–14. https://doi.org/10.1061/(ASCE)MT.1943-5533.0003634

38. ASTM C1074. Standard practice for estimating concrete strength by the maturity method. West Conshohocken, PA: ASTM

39. ASTM C109/C109M. Standard test method for compressive strength of hydraulic cement mortars (Using 2-in. or [50-mm] Cube Specimens), West Conshohocken, PA: ASTM

40. Freiesleben Hansen P, Pedersen EJ (1985) Curing of concrete structures. Draft DEB—guide to durable concrete structures. Comité Euro-International du Béton, Lausanne, Switzerland

41. Klemczak B, Batog M (2016) Heat of hydration of low-clinker cements. Part I. Semi-adiabatic and isothermal tests at different temperature. J Therm Anal Calorim 123:1351–1360. https://doi.org/10.1007/s10973-015-4782-y

42. Sakai E, Miyahara S, Ohsawa S, Lee SH, Daimon M (2005) Hydration of fly ash cement. Cem Concr Res 3(6):1135–1140. https://doi.org/10.1016/j.cemconres.2004.09.008

43. Singh NB, Kalra M, Kumar M, Rai S (2014) Hydration of ternary cementitious system: Portland cement, fly ash and silica fume. J Therm Anal Calorim 119(1):381–389

44. Nocuń-Wczelik W, Pacierpnik W, Kapeluszna E (2021) Application of calorimetry and other thermal methods in the studies of granulated blast furnace slag from the old storage yards as supplementary cementitious material. J Therm Anal Calorim. https://doi.org/10.1007/s10973-021-11161-y

45. Carino NJ, Tank RC (1992) Maturity functions for concretes made with various cements and admixtures. ACI Mater J 89(2):188–196